

# Journal of Biomedical Optics

[SPIEDigitalLibrary.org/jbo](http://SPIEDigitalLibrary.org/jbo)

## **Staining-free malaria diagnostics by multispectral and multimodality light- emitting-diode microscopy**

Aboma Merdasa  
Mikkel Brydegaard  
Sune Svanberg  
Jeremie T. Zoueu

# Staining-free malaria diagnostics by multispectral and multimodality light-emitting-diode microscopy

Aboma Merdasa,<sup>a,b</sup> Mikkel Brydegaard,<sup>a</sup> Sune Svanberg,<sup>a,c</sup> and Jeremie T. Zoueu<sup>d</sup>

<sup>a</sup>Lund University, Atomic Physics Division, P.O. Box 118, SE-221 00 Lund, Sweden

<sup>b</sup>Lund University, Department of Chemical Physics, P.O. Box 124, SE-221 00 Lund, Sweden

<sup>c</sup>South China Normal University, Center for Optical and Electromagnetic Research, University City Campus, Guangzhou 500056, China

<sup>d</sup>Laboratoire d'Instrumentation Image et Spectroscopie, INP-HB, DFR-GEE, BP 1093 Yamoussoukro, Côte d'Ivoire

**Abstract.** We report an accurate optical differentiation technique between healthy and malaria-infected erythrocytes by quasi-simultaneous measurements of transmittance, reflectance, and scattering properties of unstained blood smears using a multispectral and multimode light-emitting diode microscope. We propose a technique for automated imaging, identification, and counting of malaria-infected erythrocytes for real-time and cost-effective *parasitaemia* diagnosis as an effective alternative to the manual screening of stained blood smears, now considered to be the gold standard in malaria diagnosis. We evaluate the performance of our algorithm against manual estimations of an expert and show a spectrally resolved increased scattering from malaria-infected blood cells. © The Authors. Published by SPIE under a Creative Commons Attribution 3.0 Unported License. Distribution or reproduction of this work in whole or in part requires full attribution of the original publication, including its DOI. [DOI: [10.1117/1.JBO.18.3.036002](https://doi.org/10.1117/1.JBO.18.3.036002)]

Keywords: malaria diagnostics; multispectral imaging; microscopy; light-emitting diodes; image processing; medical imaging.

Paper 12659R received Oct. 3, 2012; revised manuscript received Dec. 28, 2012; accepted for publication Feb. 1, 2013; published online Mar. 1, 2013.

## 1 Introduction

Malaria continues to ravage the developing world and remains one of the major world-health problems (World Health Organization). Rapid, low-cost, easy-to-use, and sensitive malaria-diagnostic technologies are considered to be the effective alternatives to fight the overuse of drugs. When malaria infection is clinically suspected, subsequent overuse leads to the increase of drug resistance of the parasite, which is currently observed in the malaria abatement.<sup>1</sup> The precise identification of the malaria parasite, and its staging, will definitely facilitate its treatment with appropriate drugs. Many efforts have been made in the technological development for rapid and quantitative diagnosis of malaria.<sup>2-5</sup> Several optical approaches have also been explored<sup>6-9</sup> focusing on the detection of the malaria pigment *hemozoin*, which results from bio-crystallization of the toxic-free *heme* released by the parasite in its food vacuole, thus being a characteristic for a malaria infection. These techniques often require expensive equipment and well-equipped laboratories, which make them unrealistic on a large scale in malaria-endemic areas.<sup>10</sup> Despite the increasing number of sophisticated technologies, Giemsa staining of thin and thick blood smears remains the gold standard for malaria diagnosis.<sup>11,12</sup> Due to the transparency of the infected erythrocytes [red blood cells (RBCs)], under bright field microscopy, a dye agent is required to enhance the visual contrast of the parasite and its various shapes for accurate identification. Fluorescence staining techniques can, under optimum conditions, detect 20 to 50 parasites/ $\mu\text{L}$ ,<sup>11</sup> but is rather time-consuming and requires well-trained personnel; moreover, it requires manual examination using high-power microscopy of typically hundred fields of

the slide for providing a confident decision. In order to get precise results, the dye needs to be replaced between two to three times, which is rarely fulfilled leading to inaccurate diagnosis and thereby to presumptive treatment.<sup>13</sup> Due to the high dependence on the laboratory staff operator, it causes a number of false positive/negative smears. The disadvantage of fluorescence microscopy in malaria detection comes from the protocol of staining the blood smear and the manual examination of many fields to count, identify, and interpret the slides. The highest sensitivity of this method is only reached by well-trained microscopists. The current optical techniques also include wide-field confocal polarization microscopy,<sup>14</sup> laser desorption mass spectroscopy (LDMS),<sup>15</sup> third harmonic generation imaging,<sup>16</sup> and magneto-optical testing.<sup>17</sup> These techniques overcome some of the issues of specificity and sensitivity but are inappropriate for realistic employment in the developing parts of the world, since they likewise require expensive equipment and proper expertise. Another approach has been to develop antigen-based rapid diagnostic tests (RDTs), which can be self-administered outside the laboratory. There is contradicting information with regard to the sensitivity of antigen-based techniques<sup>11</sup> versus microscopy,<sup>12</sup> but the reports agree on the fact that the cumulative costs for administering the test on a wide scale poses a monetary problem, since the cost of a test ranges between \$0.50 to \$1.50. Since nearly 500 million cases of malaria are reported on a yearly basis, all the above-mentioned factors must be optimized in order to tackle the problem head on. An indirect problem caused by not being able to administer reliable tests is that common fever due to other infections is misinterpreted as symptoms of malaria infection. As an effect, anti-malarial drugs are used in cases where they are not needed, creating a risk that the parasite develops a resistance to the drugs.<sup>11</sup>

An RBC is about 7  $\mu\text{m}$  in diameter and roughly 2  $\mu\text{m}$  thick.<sup>18,19</sup> RBCs are unique from other cells in the body

Address all correspondence to: Aboma Merdasa, Lund University, Atomic Physics Division, P.O. Box 118, SE-221 00 Lund, Sweden. Tel: +46462224848; Fax: +46462224119; E-mail: [aboma.merdasa@chemphys.lu.se](mailto:aboma.merdasa@chemphys.lu.se)

since they have no internal structure and can therefore deform quite easily, which is important for them to easily flow through small vessels and capillaries. Blood carries many signs of possible diseases, and since haemoglobin is one of the strongest absorbers of light in the human body,<sup>19–21</sup> there is a great motivation to use optical methods to explore the potential for disease discovery. Some diseases, including malaria, will affect the cell morphology and its dynamic properties,<sup>22</sup> which may be useful in diagnosing infections. Haemoglobin is the main constituent in the RBC and its optical properties have been well characterized over a broad spectral range.<sup>18,23</sup> In the absorption spectrum there is a strong absorption band at 405 nm; the Soret band of haemoglobin. The scattering coefficient is dependent on the shape, orientation, and refractive-index distribution of the RBC since the scattering cross-section will vary across the disc-shaped RBC.<sup>12,19,24,25</sup> The refractive index is related to the absorption coefficient through the Kramer-Kronig relation.<sup>26</sup> In a thin film on a microscopy slide, there is ideally one layer of RBCs deposited, and single scattering by light can be assumed, whereas from a thick blood film having multiple layers of RBCs, multiple scattering is expected. Optical properties of whole blood have been studied extensively in relation to photo migration in the field of tissue optics.<sup>27</sup> Thin and thick films serve to extract different characteristics from a sample, where a thin smear is better for identifying the level of parasitaemia as well as the specificity, and a thick smear is better for detection since there are multiple layers and therefore more RBCs.<sup>10</sup> In the optical region, the type of scattering phenomenon is generally modelled with Mie scattering since the dimensions of an RBC is roughly one order of magnitude larger than the wavelength used to interrogate it.<sup>19,24</sup> However, when applying this scattering model, the RBC is assumed to be spherical, which in reality it is not. This becomes evident in the difference seen between the forward-scattered and back-scattered light where there is a strong angular dependence on the incident light.<sup>24,28</sup> Hemozoin, being the key substance in the existence of a malaria infection, has also been shown to exhibit strong backscattering at angles of roughly 150 deg to 160 deg to the optical axis.<sup>12</sup> These factors will complicate the interpretation of the recorded scattered light, especially if RBCs do overlap in the blood smear,<sup>29</sup> but this scattering phenomenon can also give clues as to how experiments can be conducted in more clever ways to find better contrast between healthy and malaria infected samples (i.e., which angles to record the signal). Previous work shows that an increase in the plasma osmolarity (plasma concentration in whole blood) increases the absorption coefficient and at the same time decreases the scattering coefficient for red light at 632 nm. Similarly, the hematocrit level (% of RBCs in the blood) will independently affect the scattering and absorption properties.<sup>18</sup>

In the present work, we apply multispectral and multimodal light emitting diode (LED) microscopy to investigate modes of optimal contrast in thin blood smears by simultaneous differentiation between healthy and infected blood cells employing transmittance, reflectance, and scattering recording geometries. These recording geometries comprise what we from now on will refer to as the angular modes of acquisition of the microscope. With this technique, we overcome the transparency of an RBC seen in bright-field microscopy since we are extending the spectrum of investigation to ultraviolet (UV) and infrared (IR). Optical spectra are extracted from individual blood cells in the multispectral images of all angular modes and show different

characteristics between different blood cells. Advanced clustering algorithms are employed, and the outcome is compared with the evaluation of an expert in the field. The proposed technique is based on inexpensive and realistic technology where contrast is created using 13 sequentially selected illuminating LEDs over a broad spectral range from UV to IR. The results presented in this paper are from a measurement campaign held at Laboratoire d'Instrumentation Image et Spectroscopie in Yamoussoukro, Ivory Coast in 2009.

## 2 Experimental Setup and Methods

### 2.1 Sample Preparation

Blood samples were prepared and delivered from the local clinic in Yamoussoukro, Ivory Coast. Blood smears were prepared by putting a drop of blood on an empty microscope slide and carefully spreading it with another microscope slide. They were prepared by the physicians at the clinic where no further chemicals were added to the sample. The samples were imaged within a few hours after preparation, and the peripheral areas of the smear were observed since they exhibit a single layer of RBCs.

### 2.2 Imaging System

Images were acquired using a multimode, multispectral imaging system developed by our group and presented in Ref. 30. In this system, 13 LEDs were used to selectively illuminate the sample at 13 different wavelengths ranging from UV to near infrared (NIR) (380 to 935 nm). The sample was illuminated in three angular geometries thus providing transmittance, reflectance, and scattering information. In effect, the data from the sample were recorded in 39 different ways. An overview of the system specifically showing how the sample is illuminated in the three angular modes can be seen in Fig. 1. The effective detection regions of the system are also shown here.

The camera used was a 5MPix (2592 × 1944) monochromatic CMOS camera (Guppy-503B, Allied Vision Technology, with a MT9P031 sensor from Micron/Aptina) with individual pixel size of 2.2 × 2.2 μm, each having a 12-bit pixel depth. In order for the broad spectral range to be imaged at the fixed image plane of the imaging chip, dispersion was minimized by using quartz lenses and a reflecting objective (Edmund Optics, NT58-421) with 15× magnification and 28 NA, giving an estimated point spread function (PSF) range of 67 to 1.68 μm for the wavelength range used. The illumination to measure scattering was accomplished through a fiber-optic ring light (Edmund Optics, NT54-176) device (FRL) where the light emerges at the circumference of a circle situated at a certain distance below the sample. The fibers inside the ring are tilted inward so that the light field converges at the distance of the sample.

There are two important things to note regarding the ability of the system to collect light, and they are in regard to the reflecting objective and the FRL. The objective has a Cassegrainian type of telescope arrangement, where essentially a concave and a convex mirror work in conjunction to magnify the light. In this configuration, the convex mirror surface is located directly on the optical axis and thus blocks part of the light in all angular modes (see Fig. 1). Regarding the FRL, light emerges at a tilt angle of 37 deg to the normal from the circumference of a circle having a diameter of 22 mm. Therefore, changing the height of this source in relation to the sample will change the angle at

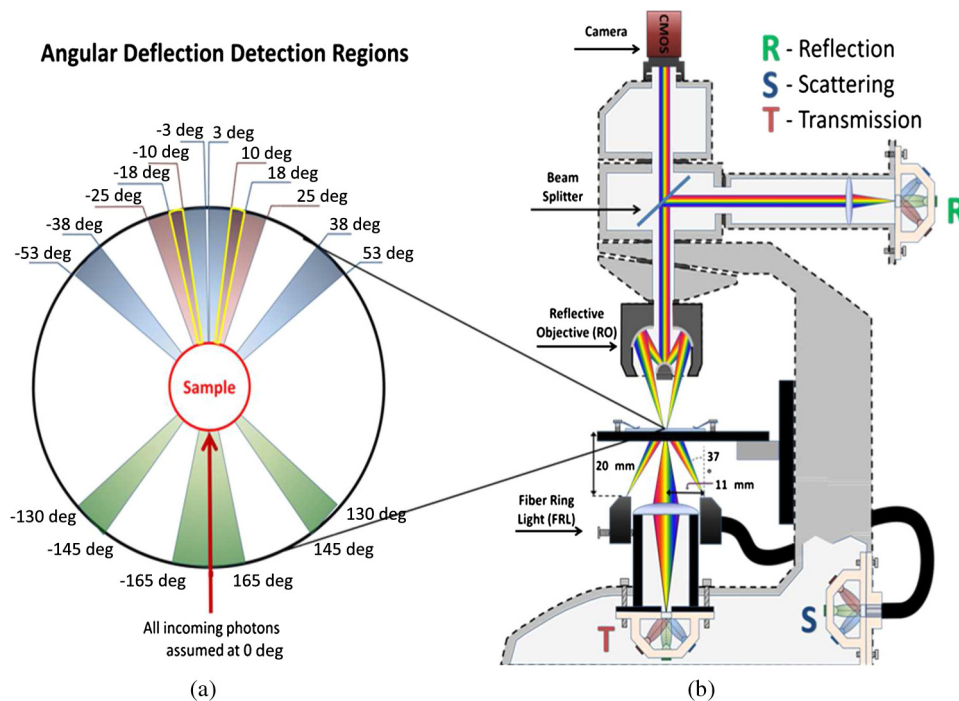


**Fig. 1** (a) Diagram of angular lobes with an overlapping region indicated by yellow lines. The color representation stands for the different detection regions for reflection (green), scattering (blue), and transmission (red). The angles represent the angles into which all incoming photons are deflected and are independent of from which angular geometry they emerge. (b) Overview of the imaging system showing a vertical cross-section of the microscope with arrangements for each angular mode (R, S, and T) indicated. In each illumination battery there are nine LEDs with 13 bands illuminating one and the same spot (only three are drawn) where an opal diffuser is placed in order to give an even distribution of light from each LED and remove angular dependence of the incident LED illumination within the battery. The rainbow of colors is a representation of a broad illumination range, and the RGB-color for the LEDs is simply to indicate that each LED is quasi monochromatic and is not representative of the actual illumination from that specific location.

which light impinges on the sample. This height was set at 20 mm during the experiment, which provided the detection sensitivity regions demonstrated in Fig. 1. These aspects, with regard to the objective and FRL, should be taken into account when analyzing the scattered light from malaria samples. There is an overlap of detection regions between transmission and scattering indicated with yellow lines. These can be adjusted to overlap less by moving the FRL in the vertical direction; however, this was not realized at the time the measurements were made.

The different angular modes complement each other providing essential information, but each also suffers some disadvantages. The transmittance mode yields good assessment of absorption properties but low contrast for transparent constituents. The reflectance mode provides an indirect measurement of the sample's refractive index as well as the surface orientation and thus curvature of the RBCs while the high reflectance from the microscope sample slide provides a low contrast. Internal structural properties of the RBCs can be revealed in the scattering mode although the illumination efficiency is low. However, this can be improved by proper collimation of the ring light. In summary, the transmittance mode provides information of the chemical composition of the RBCs, reflectance is related to the outer shape, while scattering provides information about the internal organelles such as parasites. The concept of a multi-angular mode system, sampling the scattering phase function at multiple intervals, was of key importance in the optical design in order to acquire the angularly and spectrally rich information from single scattering. This advantage becomes less significant

when approaching the diffusing regime for thick or highly scattering samples where the information about the original direction of propagation is lost during the multiple scattering events. In single scattering, we are able to observe the internal structures with improved contrast arising from surfaces with different refractive indices. Increased contrast by single scattering has also been demonstrated from crystalline hemozoin at certain angles of backscattering.<sup>12</sup>

### 2.3 Image Acquisition

The system was controlled from a PC using a custom-made program in LabVIEW™ (National Instruments, NI) where images were captured and saved in 16-bit unsigned integer images in TIFF format. For each illumination wavelength, a bright and a dark reference image was acquired, but, depending on which angular geometry was used, these recordings were done differently. For transmittance and reflectance measurements, the bright reference was an empty microscope slide placed in the object plane, whereas for scattering measurements an opal diffuser was used. Camera exposure times and gains were adjusted to give the highest intensities in the image without saturating the bright references. The dark reference images for transmittance and reflectance were taken by disconnecting the illumination current and using the same exposure times as for the bright references. For the scattering dark reference, the opal diffuser was simply removed and acquisition parameters for the scattering bright references were used. All acquisition parameters were set with the bright references, after which the sample was placed in the object plane and imaged for all three angular geometries.

It was of importance to acquire all sample images for all geometries consecutively, keeping the sample in the same location in order to compare transmittance, reflectance, and scattering properties of single RBCs.

## 2.4 Image Analysis

Once all images were taken and saved, they were analyzed using a customized algorithm in MatLab® (MathWorks). Initially, the background images were subtracted from all sample images. Then the normalization procedure was made differently for the three angular modes. For scattering, the dark reference image ( $\text{Im}_D$ ) was subtracted from the sample ( $\text{Im}_S$ ) and the bright ( $\text{Im}_B$ ) reference images. Then the sample image was divided by the bright reference image to obtain the normalized image ( $\text{Im}_{\text{Norm}}$ ) according to Eq. (1):

$$\text{Im}_{\text{Norm}} = \frac{\text{Im}_S - \text{Im}_D}{\text{Im}_B - \text{Im}_D}. \quad (1)$$

For reflectance and transmittance, an algorithm was written to automatically find the regions in the sample image where there were no RBCs. A two-dimensional (2-D) polynomial fit was applied with the intensity values in these regions; thus, a virtual bright reference image was extracted from the sample image and Eq. (1) was used. In this flat-field calibration, the intensity values given for each pixel were normalized with respect to the nearest empty region, which means the image is in effect not normalized to the microscope slide only, but to the regions free from RBCs. Normal human blood consists of 55% plasma (90% water and 10% proteins) and 45% cells,<sup>12,23</sup> which suggests that the normalization is made not only to the microscope slide but also to some plasma residue. Finally, to remove noise, a 2-D median filter was applied to the normalized images.

Following the normalization, the centers of all RBCs were manually selected in the entire image, since we did not have a trained algorithm to find them automatically. Once the spectral fingerprints of infected cells have been determined, this step can be automated. For each RBC, the spectrum for reflectance, scattering, and transmittance was extracted and concatenated into one vector having 39 elements (3 geometries  $\times$  13 $\lambda$ ). Spectra for 453 RBCs were extracted and singular value decomposition (SVD) was used.<sup>31</sup> SVD is a multivariate technique where the data are transformed into a new hyper-dimensional coordinate system where variance is maximized along each dimension representing a specific variable. From the transformation of the original data ( $\mathbf{M}_{n,\lambda}$ , where  $n$  represents a specific RBC out of a total number of  $N$  RBCs, and  $\lambda$  the wavelength), three arrays can be extracted, where base-spectra ( $\mathbf{V}_{\lambda,m}$ , where  $m$  represents the spectral component), eigenvalues ( $\mathbf{\Sigma}_{m,m}$ ) and linear coefficients ( $\mathbf{U}_{n,m}$ ) represent the original data according to Eq. (2),

$$\mathbf{M}_{n,\lambda} = \mathbf{U}_{n,m} \mathbf{\Sigma}_{m,m} \mathbf{V}_{\lambda,m}^*. \quad (2)$$

The base-spectra, also called loadings, are a new set of base functions of the original data, which are all orthogonal to each other. Because of the orthogonality between all vectors within  $\mathbf{V}$ , they represent the original data much more efficiently where the first column in this matrix represents the most significant spectral component, the second column the second most significant, and so on. Therefore, the first base-spectrum resembles the average of all original spectra for the RBCs over all

wavelengths, naturally so since the average is the best summary of all data.  $\mathbf{\Sigma}$  contains the eigenvalues for each eigenvector representing the importance of each eigenvector in relation to the others. This allows for removal of the eigenvectors that provide no additional contrast.  $\mathbf{U}$ , also called scores, contains the linear coefficients for each RBC explaining how much of each eigenvector is required in order to recreate the original spectrum for that RBC. With this information, we can reduce our original data to represent the significant contrast with only a few base-spectra rather than all contained in the original data by the removal of insignificant variables for the desired contrast. Adding more dimensions will not provide any additional contrast but only increases the noise and reduces the potential contrast of the outcome. In our case, each eigenvector represents one LED for a specific angular geometry, thus giving us 39 PCs (principal components). Not all illumination bands gave a strong contrast between the cells, and this became evident using SVD.

Hierarchical clustering and dendrogram representation<sup>32</sup> were applied to summarize the interdistance of the SVD scores to see if there were any discrete clusters of data points in the new coordinate system and how related these were. The number of dimensions from the SVD analysis was truncated to 3; thus, the algorithm clustered all 453 data points into an equal number of clusters. The number of clusters was chosen to equal the number of dimensions because we essentially select to observe the data with a reduced number of observations (dimensions).<sup>32</sup> If the number of clusters is greater, the observations would no longer be linearly independent, and we would have to account for factors that are not observed from the reduced data. From each data point, a line is drawn to all the other data points in this new Euclidian space, and the length determines how related they are. The shorter the line, the greater the chances that two points belong to the same cluster or that they are from two closely related clusters. This information is presented in a dendrogram, which gives an overview of how close the clusters are to each other in the Euclidean space. From this dendrogram, the RBC coordinates belonging to each group can be marked in the original image and the average spectra for all clusters can be extracted, plotted, and compared with each other.

## 3 Results

The results will be presented with the notion that we do not know which cells are infected and which are healthy. Rather, we will focus on finding the spectral differences between the RBCs through SVD and hierarchical clustering. We do know that the sample is infected, but which RBCs belong to which category will be left for the discussion section.

### 3.1 True-Color Representation of Single RBCs

Measurements were taken at the following wavelengths: 380, 405, 430, 480, 525, 600, 630, 660, 700, 760, 810, 850, and 935 nm in transmittance, reflectance, and scattering. Using MatLab, true-color representations of the sample were constructed by combining the normalized images taken at 630 nm (red), 525 nm (green), and 480 nm (blue) (Fig. 2). Thus the images appear as if one would manually observe them through the microscope binocular under white light illumination. Figure 2 shows the same region of the sample in all three angular modes. Since all measurements for the three angular modes were taken without moving the sample, one can compare the three modes in each pixel. However, the effective pixel-size is far below the diffraction limit set by the imaging system.

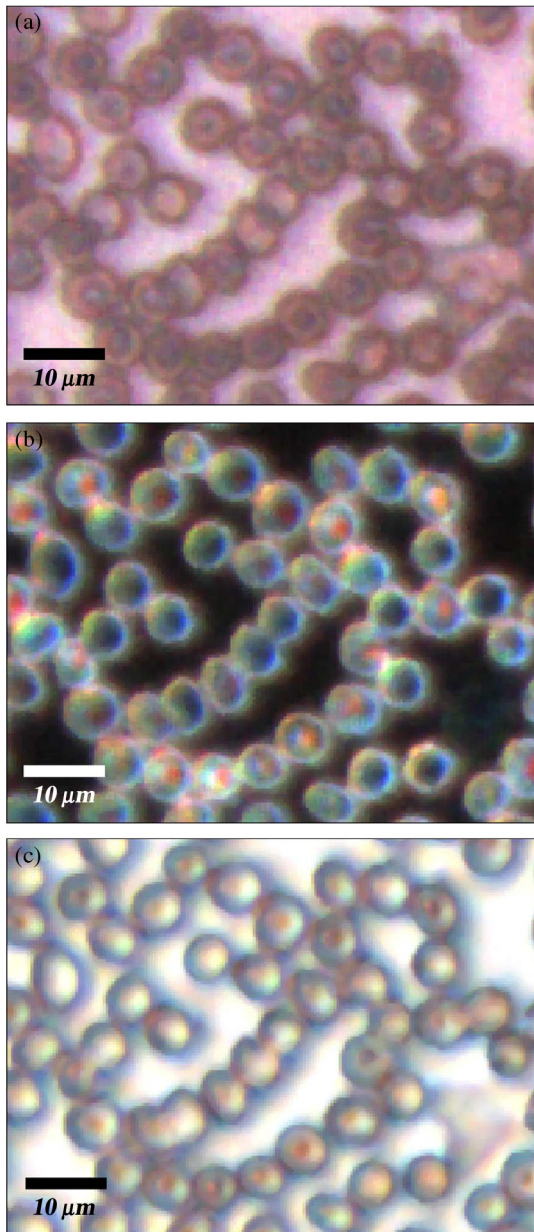


**Fig. 2** (a) to (c) True-color representation of the images taken for the three angular modes where spectral differences are seen in all, but to different degrees. 2(a) (reflection) shows the decrease in reflection in some RBCs where the central region appears darker, which can be attributed to the typical doughnut-shape of RBCs. 2(b) (scattering) shows the largest contrast between the RBCs. 2(c) (transmission) shows some RBCs absorbing more light than others in a centralized region, thus appearing as darker spots. The central red dot is most clearly visible in the scattering geometry.

This means one pixel is affected by a number of near-lying pixels and can therefore not be considered individually. However, evaluating the RBC as a whole, one can argue that pixels from different parts of the RBC play different roles in the differentiation between healthy and infected cells. Therefore malaria criteria should be applied on a pixel level but evaluated on a whole cell level; in Fig. 2 we can clearly see the RBCs to be distinctly separated. The following images show a cropped out region from the original image to better show the appearance of individual RBCs; however, all analysis was made on the full image containing 453 RBCs. It becomes evident from these true-color

representations that there are significant differences between RBCs in all three geometries, but for different reasons.

In Fig. 2(a) (reflection) we can see the expected red color of the RBCs, but there is a clear distinction between the cells. Some cells appear slightly brownish whereas others appear redder. The contrast is most evident in Fig. 2(b) (scattering) where we can clearly see the RBCs seemingly having an internal structure. Those without internal structure appear to have hollow centers whereas those having something concrete inside scatter significantly. In the acquisition for scattering, the FRL is aligned so that in the absence of a sample, the majority of the light passes outside the aperture of the objective. Thus, when there is something in the sample plane deflecting the light from its original path into the aperture of the objective, a signal is measured from what we define as zero, being the dark reference. In Fig. 2(c) (transmission) the light passes through the RBCs, and we can observe a reduced transmittance from some cells compared with others. There is an apparent darker region in the center of some RBCs, which seems to slightly change from cell to cell. One reason why the cells appear white rather than red is because they have been normalized to the regions free from cells. These regions contain blood plasma, which has similar spectral characteristics as haemoglobin,<sup>23</sup> and thus the RBCs appear white rather than red. In this aspect, the transmission sample would not appear as it does in Fig. 2(c) to the human eye. What is interesting is that Fig. 2(a) is also normalized to the region free from RBCs, but there is a larger contrast due to the scattering properties of RBCs where the back-scattered light is significantly stronger when the light is incident at an angle to the normal of the RBC surface,<sup>24</sup> which, according to Fig. 1, cover the photons that are deflected at angles between 35 deg to 50 deg and 0 deg to 15 deg from their incidence. We also see that the angular sensitivity regions for transmission lie close to the optical axis as these photons are not deflected far from it. This is another contributing reason to why higher intensities can be measured from the cells compared with the white reference (empty slide) as the forward-scattering property of individual RBCs tends to increase the intensity when the angle of the incident light approaches the plane perpendicular to the optical axis.<sup>24</sup>

Comparing all angular modes, we can see that the invisible characteristics in transmission become clearly visible in scattering. In general we see that the differences of the cells in each angular mode correlate well between the angular modes; the same RBC having a brown spot in Fig. 2(c) (transmission), appears browner in Fig. 2(a) (reflection), and has a red spot in the center of Fig. 2(b) (scattering). From the three images in Fig. 2, we can draw a conclusion that some RBCs have some sort of internal structure, which will be discussed further below. According to the life-cycle of the *Plasmodium falciparum* parasite, where during its trophozoite stage it enters the RBCs and grows within, we can expect to see the infected cells having some sort of internal structure.<sup>11</sup> We keep this in mind as we continue to apply statistical methods for all RBCs in all geometries and spectral bands.

### 3.2 Singular-Value Decomposition and Hierarchical Clustering

Before any further analysis was made, the spectra had to be collected from the RBCs. This was done by cropping out a region with a three-pixel radius from the center of the RBC, over which an average intensity was acquired at each spectral band. Thus a spectrum for every RBC in each geometry was

extracted at a spectral resolution of 13 bands from 380 to 935 nm. In order to perform the SVD analysis, we had to concatenate the spectra from the three different geometries into one for each RBC, which is seen in Fig. 3(a). In this plot we can see the general trend of how not only the spectral characteristics change throughout the three angular modes, but also the variance between the blood cells. In Fig. 3(b) we see the

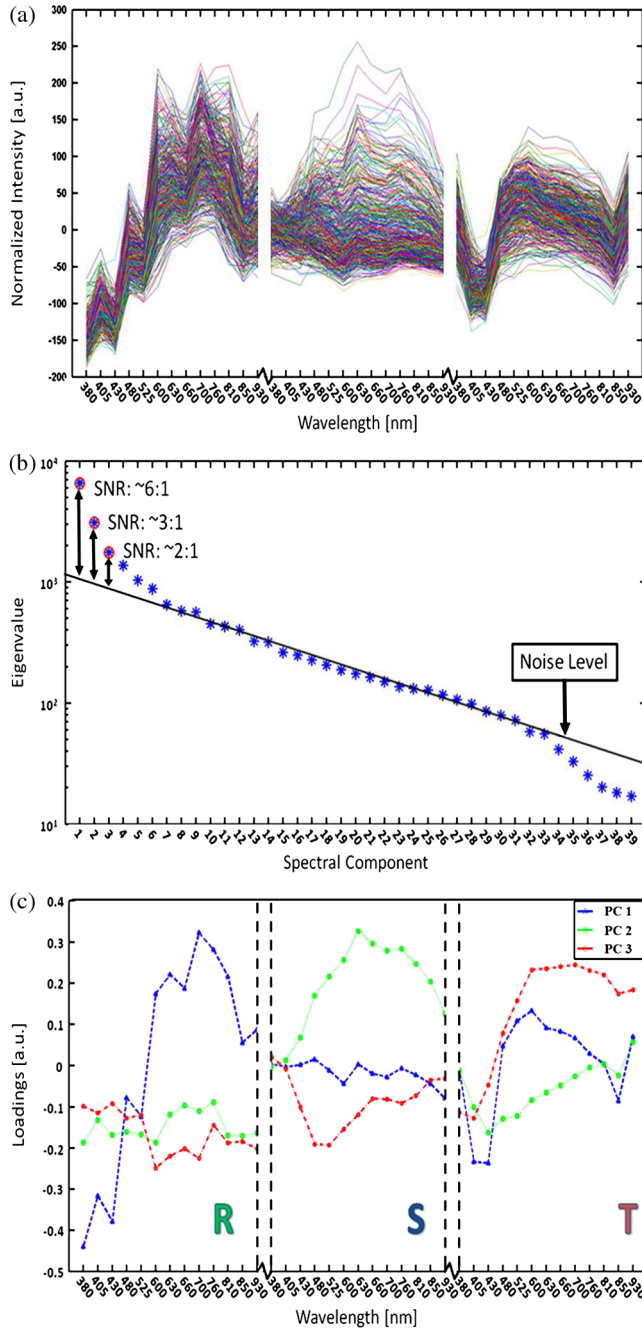


**Fig. 3** (a) shows the collection of spectra from all RBCs concatenated between the three angular modes. The rather large variance becomes evident. Figure 3(b) shows the eigenvalues for each PC where the first three are considered to be most relevant as their SNR is 2:1 or higher. The noise level is indicated with a black line drawn through the apparent plateau. The y-scale is logarithmic. Figure 3(c) shows the first three base-spectra for all PCs, and it is evident that the original data can be represented quite well with these curves. The spectra have been divided up in the angular modes.

extracted eigenvalues, which are the diagonal elements of  $\Sigma$ , once SVD has been applied. To determine where to truncate our data, we had to study the relevance of the signal of each  $\Sigma$  in comparison to what we define as noise or, rather, irrelevant information. The noise level was chosen from the apparent plateau in Fig. 3(b), where a black line is interpolated through the plateau. Based on this noise level,  $\Sigma_{1,1}$  gives a signal-to-noise ratio of approx. 6:1,  $\Sigma_{2,2}$  approx. 3:1 and  $\Sigma_{3,3}$  slightly less than 2:1. We decided that this was the lowest we would go before adding another PC did not provide additional relevant information. Therefore, the first three  $\Sigma$  were used as indicated by the three red circles in Fig. 3(b). In Fig. 3(c) the first three base-spectra are plotted in different colors, and they are separated into their respective angular geometry. Comparing Fig. 3(a) and 3(c), we see that from the first three base-spectra we can more or less describe all the original spectra for the RBCs in different linear combinations. How much of each eigenvector we use is indicated in  $\mathbf{U}$  for each RBC, and we recreate the original spectra from the reduced set of coordinates according to Eq. (2),

$$\mathbf{M}_{n_{1..N}, \lambda_{1..A}} = \mathbf{U}_{n_{1..N}, m_{1..tr}} \Sigma_{m_{1..tr}, m_{1..tr}} \mathbf{V}_{\lambda_{1..A}, m_{1..tr}}^*, \quad (3)$$

where  $N$  represents the total number of RBCs ( $N = 453$ ),  $\Lambda$  represents the total number of spectral bands ( $\Lambda = 39$ ), and  $tr$  stands for the number of dimensions we decided to reduce the data to, which in our case is  $tr = 3$ . Since we used only the three first eigenvectors, and the fact that they are orthogonal, makes it easy to visualize the data points in a three-dimensional (3-D) space. However, we should keep in mind that since the different eigenvectors carry different weight, the scales will be different along each dimension. Each RBC is then represented as a point in a 3-D histogram.

From the new coordinate system, the Euclidean distances between all points were calculated in order to determine which cluster they belong to. The relation between these three clusters is shown in the dendrogram in Fig. 4. On the y-axis, the values represent the distance in the Euclidian space, which was previously transformed with the SVD analysis; thus the values carry no units. Note that the color coding is not related to Fig. 3 but rather to the spectra in Fig. 5. Overall we can see that clusters 1

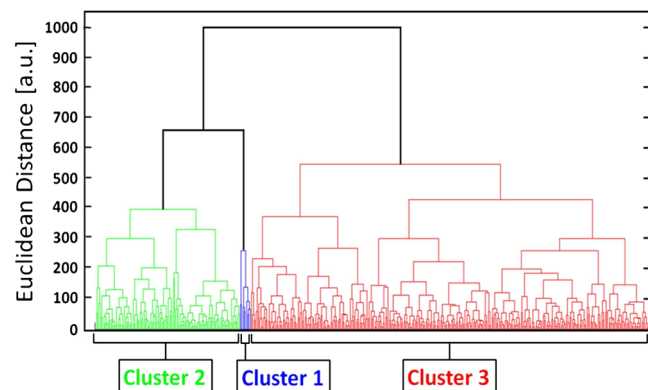


**Fig. 4** Dendrogram representation of all the RBCs and their relation according to the reduced variables from the SVD analysis. The color coding is kept for the next section where the spectra are shown for each cluster. The y-axis represents the Euclidean distance in the newly formed coordinate system and therefore carries no units. In cluster 1 there are nine RBCs; in cluster 2 there are 118 RBCs; and in cluster 3 there are 326 RBCs.

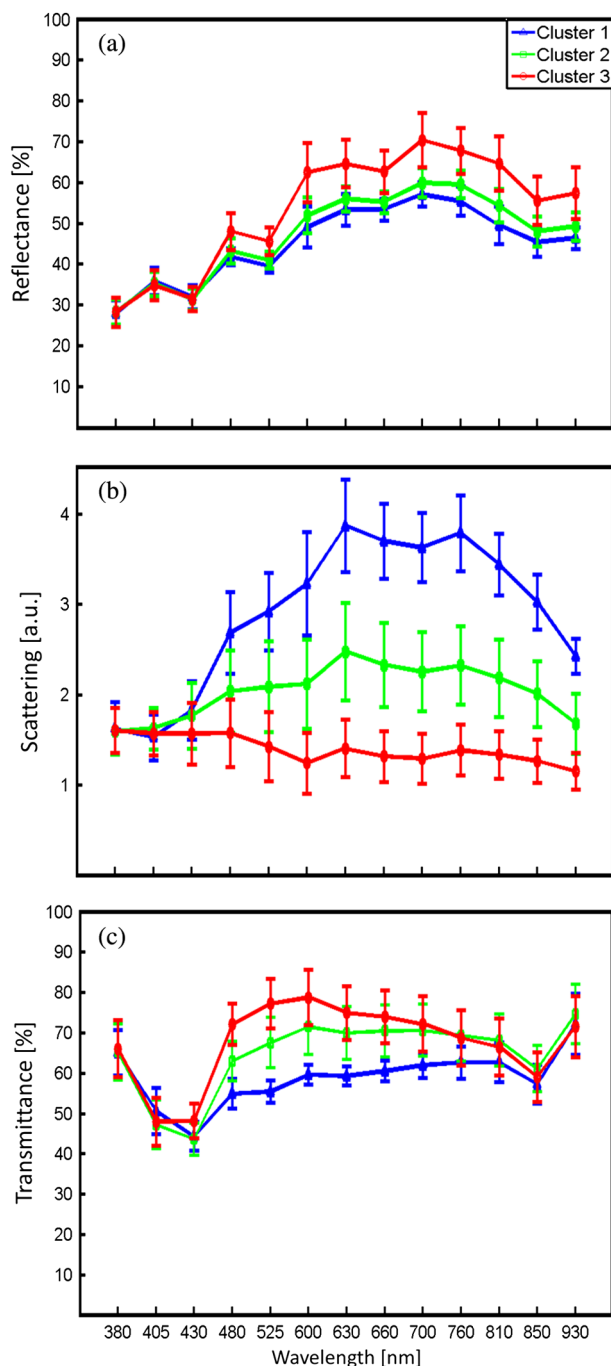


**Fig. 5** (a) to (c) Average spectra for the three clusters in the three angular modes. In all spectra we see contrast to some extent between the three clusters. 5(a) (reflectance) shows a progression from cluster 1 to cluster 3 of an increase in reflectance. 5(b) (scattering) exhibits the strongest contrast where the progression of increased scattering goes from cluster 3 to cluster 1. 5(c) (transmission) shows an increase in absorption from cluster 3 to cluster 1, which we can understand from 5(a) where we saw a decrease in reflectance in a similar fashion.

and 2 are closer related to each other than cluster 3. From the 453 RBCs examined, 9 fell into cluster 1, 118 into cluster 2, and 326 into cluster 3. Also evident in the figure are several subclusters. We chose three clusters, but there is of course a possibility that there are more variables that differentiate RBCs. However, the three clusters seem to be significantly separated to motivate a comparison of them, and this should become more evident

when examining their spectral characteristics in the following section.

### 3.3 Individual RBC Spectra in all Angular Modes

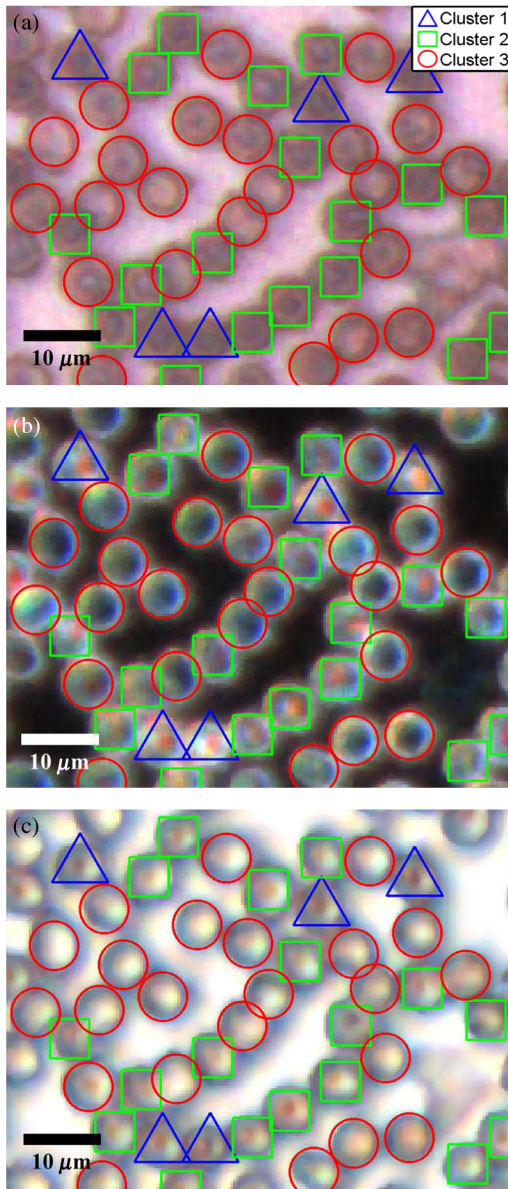
Tracing back the color space coordinates for the data points in the clusters, we took the average spectrum for each cluster and plotted them separately for each angular geometry seen in Fig. 5. In all spectra we can see some differences between the different clusters, but some promote the contrast more than others. What becomes clear is the progression as we observe all three clusters. Cluster 3 has by far more RBCs than the other two, followed by cluster 2 and, finally, very few RBCs in cluster 1. Remembering the life cycle of the malaria parasite, we note that when it enters the RBC in its trophozoite stage it consumes haemoglobin. Then it makes sense that we can see a progression as RBCs would naturally be in different stages of infection; the longer the parasite has been occupying the RBC, the more its spectral characteristics would differ from a healthy RBC. In Fig. 5(a) (reflection), we would also expect to see a decrease in reflection due to the high absorption at the characteristic Soret absorption band of haemoglobin at 405 nm, but it seems to have shifted to around 430 nm. This can partially be explained by the scattering characteristics of RBCs, which heavily depend on the shape and orientation of the cell as well as the angle of the incident light. There is a progression of increased reflectance moving from cluster 1 to cluster 3 as well as a general increase of reflectance from 480 up through 930 nm. In Fig. 5(b) (scattering), we see the largest contrast where all three clusters differ significantly from 480 nm and above, where cluster 1 and 2 seem to peak around 630 nm. It does make sense that the scattering geometry gives the strongest contrast because not only the parasite, but also the hemozoin that it expels, has structure providing contrast with regard to a healthy cell containing only haemoglobin.<sup>27</sup> The changing of spectral characteristics is most apparent in scattering going from cluster 1 to cluster 3, where scattering significantly increases for all wavelengths above 430 nm. In Fig. 5(c) (transmission), we see the characteristic Soret absorption of haemoglobin clearly at 405 nm, which appears to be at more or less the same level in all clusters, with perhaps a slight increase in absorption for clusters 1 and 2. What is more apparent in transmission is the increased absorption over the spectral region 480 to 810 nm as we move toward cluster 1 from cluster 3. The increased absorption can be paralleled with the decreased reflectance comparing the clusters.

### 3.4 Mapping of Cluster Classifications onto RBCs

Once the three clusters were determined, the respective coordinates were marked on the true-color images to get a visual perception of how the different RBCs would appear to the human eye if observed directly through the binoculars of a microscope. Figure 6 is the same as Fig. 2, but having all RBCs marked with their respective cluster where cluster 1 is represented with a blue triangle, cluster 2 with a green square, and cluster 3 with a red circle. Note that some RBCs are not marked at all since they were not counted in the original list for reasons such as lying too close to a border or having an odd shape. Note also that the analysis was applied to the full image where Figs. 2 and 6 only shows a small region for better visibility.

In Fig. 6(a) (reflection), we see a distinct contrast difference between the clusters, but it is not as clear as for the other two other angular modes. This we can understand from the results in





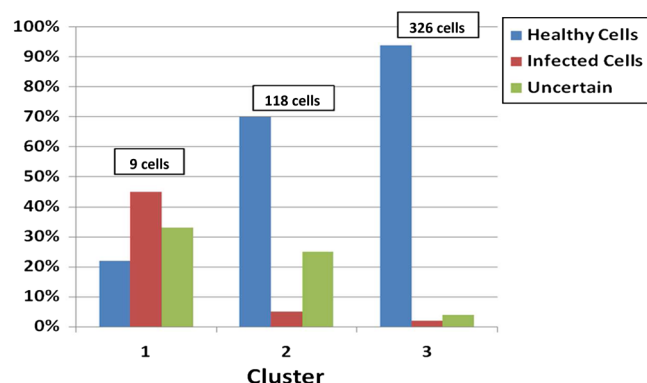
**Fig. 6** (a) to (c) From the three different clusters marked in this true-color image, we see significant distinctions in all angular modes, where the largest is again seen in scattering. 6(a) (reflectance) only shows a small, but still significant variance between the different clusters. It is more evident in 6(b) (scattering) as well as 6(c) (transmission). Cluster 1 is clearly distinct from cluster 3 in 6(b), which was already evident in Fig. 5(b). Some of the markings are not centered, which is due to the initial selection not being exactly in the middle of the RBC, but due to the cropped out region being significantly smaller than the RBC, it should not play a significant role.

Fig. 5(a), where the reflectance spectra do not show large contrast between the clusters. However, we can see significant differences between the general appearances of the RBCs belonging to the different clusters. RBCs belonging to clusters 1 and 2 seem to progressively get darker and browner compared to the RBCs in cluster 3. Figure 6(b) (scattering) provides the largest contrast, as expected from the spectra in Fig. 5(b). The red spots seen in the RBC centers are clearly visible in clusters 1 and 2 and clearly not in cluster 3. Comparing cluster 1 with cluster 2, there appears to be a slight difference in visibility of the red spot. The previously discussed progression of the spectra is most

visible in Fig. 6(b) for scattering, where all RBCs belonging to cluster 1 have the brightest red spots in the center. There is also a number of RBCs belonging to cluster 2 having the bright spot but not as bright as the ones from cluster 1. All RBCs belonging to cluster 3 are lacking a red spot in the middle. From Fig. 6(c) (transmission), we see there are differences between the three clusters where there is an apparent brown spot in the center of the RBCs belonging to cluster 1 and 2, and not in cluster 3. Between cluster 1 and 2, we again see the slight difference in visibility of the spot in the center. The fact that the spot in the middle is brown in transmission and reflection and red in scattering is due to the different normalization procedure for the acquisition modes previously discussed.

### 3.5 Malaria Expert Evaluation

The blood smear was independently analyzed visually by Jeremie T. Zoueu, who has considerable experience in malaria evaluation. For all studied RBCs, he had to decide whether the RBC was infected or healthy by visual examination as each RBC was individually presented on a computer screen as shown in Fig. 2. If he was uncertain to determine an infection he could also indicate that (Fig. 7 shows a chart with the corresponding classification). The results are presented cluster by cluster where the percentage represents how many of the RBCs in that cluster belong to each expert classification. Cluster 1 has 9 RBCs, out of which 22.2% are indicated as healthy, 44.5% are indicated as infected, and 33.3% uncertain. Cluster 2 has 118 RBCs, out of which 70.3% are indicated as healthy, 5.1% infected, and 24.6% uncertain. Cluster 3 has 326 RBCs, out of which 93.8% are indicated as healthy, 1.5%, infected and 4.7% uncertain. This gives a total of 391 healthy and 15 infected RBCs with the certainty of the expert; thus, over the entire sample, our expert confirms that 3.3% are infected. Malaria parasitemia ranges depending on the severity of the infection as well as the age of the patient. The rate found from a study in 1995 was 1.6% for children aged 1 to 4 and 5.5% for patients of 15 years and up.<sup>33</sup> From this we can say that our results are acceptable. However, a proper procedure of first using our microscope and then directly after staining the sample and applying a conventional counting method was not performed. For this reason we cannot give any value of specificity and sensitivity but rather



**Fig. 7** A chart showing the distribution of healthy and infected cells for the different clusters analyzed by our malaria expert. In each cluster there is also a column indicating how many blood cells the expert could not properly distinguish. The trend becomes obvious as the number of infected cells strongly decreases as we go from cluster 1 to 3. Similarly, the number of healthy cells increases from cluster 1 to 3.

conclude that our method gives promising results in good agreement with an expert in the field having used conventional methods. We can also infer from the chart that the percentage of infected cells decreases as well as the number of healthy cells increases from cluster 1 to 3. Although the number of RBCs in cluster 1 is significantly lower than cluster three, the majority of them are infected. This is a strong indication that our routine can identify malaria-infected blood cells without the use of staining.

#### 4 Discussion

We have presented a robust and automated approach based on the optical fingerprint of RBCs and multivariate analysis to differentiate infected RBCs from healthy in an unstained positive blood smear. This technique exploits the variation of the optical properties of the constituents of the RBCs. The normalization step provides a common basis for comparison between samples of different origins. Uninfected RBCs are essentially composed of haemoglobin, and their spectra are expected to be dominated by the spectral fingerprint of haemoglobin, strongly characterized by the Soret band (412 nm) and their two additional bands at 541 and 576 nm, in transmission mode.<sup>20</sup> The various parasite stages (trophozoite, ring, schizont, or gametocyte), the presence of hemozoin, or the decrease of haemoglobin concentration, show up in all three acquisition modes, therefore giving a strong indication when an infection is prevalent. Yulia et al. have published quasi-exhaustive optical fingerprints of all stages of the *P. falciparum* as well as hemozoin spectra.<sup>34</sup> Hemozoin displays a particular absorption band at 630 and 660 nm. Wilson et al. have measured an overall decrease of the scattering probability from UV to near infrared. Cluster 2 (Fig. 5) shows the general spectral behavior of the *P. falciparum* parasite. Our approach is focused on the mean pixel value of the RBCs properties rather than specific plasmodium indicators. For this reason, the clustered spectra are examined in terms of average characteristics of the indicators above for the three modes. This spectral differentiation between healthy and infected RBCs is particularly observed by an increase in scattering, decrease in reflectance as well as a decrease in transmittance of infected RBCs compared with healthy ones. The visual differentiation of the RBCs in unstained blood smears is hard because of possible confusion between the various shapes of the RBCs in the three modes, platelets, or other residues stuck to the RBCs. The central valley of RBCs (due to its biconcave shape) can exhibit an artificial increase of scattering and absorption and a decrease of reflection similar to that of the symptoms of infection. This visual confusion is solved by spectral analysis and will be further examined. In order to extract values of specificity and sensitivity, our technique needs to be done in accordance with a lab conducting the conventional Giemsa-staining technique. The same areas of the blood smear should be viewed in both microscopes, where a proper staining procedure is conducted immediately after the multispectral microscope has been applied. Therefore we cannot draw any stronger conclusion than that our technique seems to agree well with the expert's visual analysis.

Although the development platform includes a camera for high-resolution acquisition and a computer to analyze the data, we believe that hand-held devices using only LEDs and an objective in a battery-driven box can create visible contrast to the naked eye, since it mainly comes from the selective illumination and appropriate angular geometries; this is very

realistic for the developing world especially since the contrast is instantly seen without having to prepare the sample through staining and the test can be administered without costs for biological test-strips. Using this technique with more samples and defining proper values for specificity and sensitivity, we can determine which LEDs in which angular geometry give the strongest contrast and from this create simple push-button devices, which readily detect malaria within a few seconds. We base this conclusion on the fact that we have created contrast without the use of staining and by simply selectively illuminating the sample with different LEDs in different geometries, which can be readily recreated in a more convenient manner for the field. It was also verified that when using all angular modes in the SVD analysis we get a truncation from the merged set, which essentially means we select the three overall most significant components. This was verified by estimating the spectral truncation for sets, including combinations of just two of the three modes in all possible combinations. This provided two (instead of three) principal components giving a SNR higher than 2. Using the same criterion on each single angular mode also gave a truncation of just two, and in one case only 1.

Finally, we want to acknowledge that there are improvements to be made according to the above arguments. There are a number of factors that affect the optical properties of blood such as the hematocrit level (volume fraction of cells within the whole blood volume), oxygenation of haemoglobin, which leads to changes in absorption, osmolarity changes, which affect the haemoglobin concentration and therefore indirectly changes the absorption of the RBCs. These are all discussed in Ref. 18. However, as we are already seeing a strong contrast between what apparently are infected and healthy RBCs, this study should only increase the confidence of our results.

#### Acknowledgments

We would like to extend our gratitude to many parties being involved in bringing this research forward. The International Science Programme (ISP), Uppsala University, has been supporting this research by providing funds for building six additional microscopes that are today being employed in various parts of the developing world for the purpose of solving the problem in malaria diagnostics. ISP has also funded several workshops where this research was shared amongst participating students and professors of AFSIN (African Spectral and Imaging Network). Funding has also come from the Swedish Research Council and from the Linnaeus grant through the Lund Laser Centre (LLC) to build the prototype. Much appreciation is extended to Jens Ålebring and Hiran Jayaweera for their contribution in the construction of the microscope.

#### References

1. P. B. Bloland and M. Eitling, "Making malaria treatment policy in the face of drug resistance," *Ann. Trop. Med. Parasitol.* **93**(1), 5–23 (1999).
2. P. A. Wintstanely, S. A. Ward, and R. W. Snow, "Clinical status and implication of antimalarial drug resistance," *Microb. Infect.* **4**(2), 157–164 (2002).
3. A. Moody, "Rapid diagnostic test for Malaria parasites," *Clin. Microbiol. Rev.* **15**(1), 66–78 (2002).
4. C. Wongsrichanalai et al., "A review of malaria diagnostic tools: microscopy and rapid diagnostic test (RDT)," *Am. J. Trop. Med. Hygiene* **77**(Suppl. 6), 119–127 (2007).
5. C. K. Murray, "Update on rapid diagnostic testing for malaria," *Clin. Microbiol. Rev.* **21**(1), 97–110 (2008).

6. W. G. Lee et al., "Nano/microfluids for diagnostic of infectious diseases in developing countries," *Adv. Drug Deliv. Rev.* **62**(4–5) 449–457 (2010).
7. T. Häscheid, E. Valadas, and M. P. Grobusch, "Automated malaria diagnostics using pigment detection," *Parasitol. Today* **16**(12), 549–551 (2000).
8. S. Cho et al., "Optical imaging techniques for the study of malaria," *Trends Biotechnol.* **30**(2), 71–79 (2011).
9. F. Kawamoto, "Rapid diagnosis of malaria by fluorescence microscopy with light microscope and interference filter," *Lancet* **337**(8735), 200–202 (1991).
10. M. T. Makler, C. J. Palmer, and A. L. Ager, "A review of practical techniques for the diagnosis of malaria," *Ann. Trop. Med. Parasitol.* **92**(4), 419–433 (1998).
11. P. J. Guering et al., "Malaria: current status of control, diagnosis, treatment, and a proposed agenda for research and development," *Lancet Infect. Dis.* **2**(9), 564–573 (2002).
12. B. K. Wilson et al., "Detection of malarial byproduct hemozoin utilizing its unique scattering properties," *Opt. Express* **19**(13), 12190–12196 (2011).
13. D. Lenz et al., "Assessment of LED fluorescence microscopy for the diagnosis of Plasmodium falciparum infections in Gabon," *Malaria J.* **10**, 194 (2011).
14. M. C. Campbell et al., "Confocal polarimetry measurements of tissue infected with malaria," in *Conf. Frontiers in Optics. Seeing the Invisible: Strategies for Imaging Transparent Cell Types II (FThK)*, OSA, San Jose, California (2007).
15. P. F. Scholl et al., "Rapid detection of malaria infection in vivo by laser desorption mass spectrometry," *Am. J. Trop. Med. Hyg.* **71**(5), 546–551 (2004).
16. J. M. Béglise et al., "Sensitive detection of malaria infection by third harmonic generation imaging," *Biophys. J.* **94**(4), L26–L28 (2008).
17. P. F. Mens et al., "Laboratory evaluation on the sensitivity and specificity of a novel and rapid detection method for malaria diagnosis based on magneto-optical technology (MOT)," *Malaria J.* **9**, 207 (2010).
18. A. Roggan et al., "Optical properties of circulating human blood in the wavelength range 400–2500 nm," *J. Biomed. Opt.* **4**(1), 36–46 (1999).
19. M. Hammer et al., "Single scattering by blood cells," *Appl. Opt.* **37**(31), 7410–7418 (1998).
20. E. K. Hanson and J. Ballantyne, "A blue spectral shift of the haemoglobin soret band correlates with the age (time since deposition) of dried bloodstains," *PLoS One* **5**(9), 12830–12840 (2010).
21. D. H. Tycko et al., "Flow-cytometric light scattering measurements of red blood cell volume and haemoglobin concentration," *Appl. Opt.* **24**(9), 1355–1365 (1985).
22. M. S. Amin et al., "Microrheology of red blood cell membranes using dynamic scattering microscopy," *Opt. Express* **15**(25), 17001–17009 (2007).
23. M. Meinke et al., "Optical properties of platelets and blood plasma and their influence on the optical behavior of whole blood in the visible to near infrared wavelength range," *J. Biomed. Opt.* **12**(1), 14024–14032 (2007).
24. A. M. K. Nilsson et al., "T-matrix computations of light scattering by red blood cells," *Appl. Opt.* **37**(13), 2735–2748 (1998).
25. G. S. Noland, N. Briones, and D. J. Sullivan Jr., "The shape and size of hemozoin crystals distinguishes diverse Plasmodium species," *Molec. Biochem. Parasitol.* **130**(2), 91–99 (2003).
26. D. J. Faber, "Oxygen saturation-dependent absorption and scattering of blood," *Phys. Rev. Lett.* **93**(2), 28102 (2004).
27. M. Friebe et al., "Determination of optical properties of human blood in the spectral range 250 to 1100 nm using Monte Carlo simulations with hematocrit-dependent effective scattering phase functions," *J. Biomed. Opt.* **11**(3), 34021–34031 (2006).
28. G. A. Jamjoom, "Dark-field microscopy for detection of malaria in unstained blood films," *J. Clin. Microbiol.* **17**(5), 717–721 (1983).
29. J. He et al., "Light scattering by multiple red blood cells," *J. Opt. Soc. Am. A* **21**(10), 1953–1961 (2004).
30. M. Brydegaard et al., "Versatile multispectral microscope based on light emitting diodes," *Rev. Sci. Instrum.* **82**(12), 123106 (2011).
31. G. H. Golub and C. Reinsch, "Handbook series linear algebra: singular value decomposition and least squares solutions," *Numerische Mathematik* **14**(5), 403–420 (1970).
32. A. Runemark et al., "Rare events in remote dark-field spectroscopy: an ecological case study of insects," *IEEE J. Sel. Top. Quantum Electron.* **18**(5) 1573–1582 (2012).
33. S. P. Kachur et al., "Prevalence of malaria parasitemia and accuracy of microscopic diagnosis in Haiti, October 1995," *Rev. Panam. Salud Publica* **3**(1), 35–39 (1998).
34. Y. M. Serebrennikova, J. Patel, and L. H. Garcia-Rubio, "Interpretation of the ultraviolet-visible spectra of malarial parasite Plasmodium falciparum," *Appl. Opt.* **49**(2), 180–188 (2010).